Inventory and Spatial Distribution of Landslides Triggered by the 8th August 2017 M_W 6.5 Jiuzhaigou Earthquake, China

Yingying Tian [iD][1], **Chong Xu** [iD]*[1], **Siyuan Ma**[1], **Xiwei Xu**[1,2], **Shiyuan Wang**[3], **He Zhang**[4]

1. *Key Laboratory of Active Tectonics and Volcano, Institute of Geology, China Earthquake Administration, Beijing* 100029, *China*
2. *Institute of Crustal Dynamics, China Earthquake Administration, Beijing* 100085, *China*
3. *Sichuan Earthquake Agency, Chengdu* 610041, *China*
4. *Hebei Earthquake Agency, Shijiazhuang* 050021, *China*

[iD]Yingying Tian: https://orcid.org/0000-0002-6729-773X; [iD]Chong Xu: https://orcid.org/0000-0002-3956-4925

ABSTRACT: An accurate and detailed seismic landslide inventory is essential to better understand the landslide mechanism and susceptibility. The 8th August 2017 M_W 6.5 Jiuzhaigou Earthquake of China initiated a large number of coseismic landslides. The results of the post-seismic survey show the actual landslide number might be underestimated in previous publications. Coupled with field investigation and visual interpretation on high-resolution remote sensing images before and after the main shock, we established a detailed inventory of landslides triggered by the earthquake. Results show that this event caused at least 4 834 individual landslides with a total area of 9.64 km^2. They are concentrated in an elliptical area of 434 km^2, dominated by medium- and small-scale rock falls and debris slides. Statistics indicate that, except for slope aspect that seems not significantly correlated with the landsliding, these landslides are most common in the places with following features: elevation of 2 800–3 400 m, slope angle greater than 30º, slope positions of upper, middle and flat slopes, and Carboniferous limestone and dolomite. Besides, the landslide area percentage (LAP) and landslide number density (LND) values decrease with the increasing distance to river channels and roads, implying a positive correlation. Instead of centering around the epicenter, most of these coseismic landslides are distributed along the inferred seismogenic fault, which means that the seismogenic structure played a more important role than the location of the epicenter. Remarkable differences in landslide densities along the fault indicate the varied landslide susceptibility which may be attributed to other varied controls along the fault such as the rock mass strength. In sum, this study presents a more detailed inventory of the landslides triggered by the 2017 M_W 6.5 Jiuzhaigou Earthquake, describes their distribution pattern and analyzes its control factors, which would be helpful to understand the genesis of the coseismic landslides and further study their long-term impact on the environment of the affected area.
KEY WORDS: Jiuzhaigou Earthquake, coseismic landslide, landslide inventory, influencing factors, spatial distribution.

0 INTRODUCTION

Landslide inventories are fundamental to the research of regional landslides (Li F et al., 2017; Zuo and Carranza, 2017; Feng et al., 2016; Xu et al., 2016a; Zhou et al., 2016; Harp et al., 2011). For the earthquake-triggered landslides, a complete and detailed landslide inventory is critical for studies of landslide distribution patterns, slope susceptibility assessment, post-seismic evolution of landslides, identification of the seismogenic structure of earthquakes rupturing the blind faults, and so on (Rao et al., 2017; Tian et al., 2017a, b; Yang et al., 2017; Xu et al., 2016b; Owen et al., 2008; Kamp et al., 2008; Keefer

et al., 2006; Keefer, 1984). In the early time, because of the lack of effective methods for field surveys, advanced remote sensing technologies and commonly accepted landslide-mapping principles, it was difficult to prepare detailed inventories of landslides caused by large historical earthquakes. Therefore, a few earthquake cases in recent years that have elaborated seismic landslides inventories are proper for further studies (Xu, 2018). The examples with detailed landslide inventories include major events of 1994 Northridge, America (Harp and Jibson, 1996), 1999 Chi-Chi, Taiwan, China (Lee, 2013; Liao and Lee, 2000), 2004 Niigata, Japan (Wang et al., 2007; Chigira and Yagi, 2006), 2005 Kashmir, Pakistan (Owen et al., 2008; Kamp et al., 2008), 2008 Wenchuan, China (Xu et al., 2014a), 2010 Yushu, China (Xu and Xu, 2014a), 2013 Lushan, China (Xu et al., 2015), 2013 Minxian, China (Tian et al., 2016; Xu et al., 2014b), 2015 Gorkha, Nepal (Kargel et al., 2016; Xu et al., 2016a), and 2016 Kumamoto, Japan (Xu et al., 2018a). Some common laws of seismic landslides based on these inventories

are achieved, which is helpful for understanding this kind of landslide and engineering practice in the seismic area. For example, the landslides triggered by the thrusting earthquake always are concentrated on the hanging wall of the seismogenic fault. Such laws and the spatial distribution of seismic landslides can be used to auxiliarily identify the seismogenic fault of earthquakes with no obvious surface ruptures (Xu and Xu, 2014b). Keeping eyes on the recent and future large earthquakes and preparing the detailed inventories of the landslides triggered by them, if any, remains an essential job for geosciences to understand seismic landslides and their mechanism.

On 8 August, 2017, a M_W 6.5 (Ms 7.0) earthquake occurred in Jiuzhaigou County, Aba Autonomous Prefecture, Sichuan Province, China with the location of (33.2ºN, 103.8ºE) and focal depth of 20 km. This is the third major event in the eastern of Tibetan Plateau following the 2008 Wenchuan and the 2013 Lushan earthquakes of China. A large number of coseismic landslides were triggered in the earthquake-affected area which is located in the transition zone between the plateau and basin, characterized by intensive tectonic activities and alpine gorges. In the aftermath of this earthquake, researchers scrambled to focus on these landslides. For instance, Xu et al. (2018b) presented a panorama of the coseismic landslides by integrating the data of field investigations and remote sensing images. With the regional terrain and geological data, Liu et al. (2017) carried out a rapid assessment of the landslides using the Newmark cumulative displacement model. Dai et al. (2017) and Fan et al. (2018) identified 1 883 landslides in an area of 840 km^2 around the epicenter based on remote sensing data; Wu et al. (2018) complemented these results and gave a more detailed map with 2 212 landslides. Based on their respective landslide data, they analyzed the relationship between the landslides and some control factors. These studies can help to understand the distribution pattern of landslides triggered by the Jiuzhaigou Earthquake, the assessment of slope stability and the long-term impacts on the affected area. Nevertheless, the recent field survey shows that the landsliding of this event was unusually dramatic at some sites, and the landslide linear density along some roads is even larger than 10 per kilometer (Xu et al., 2018b). What's more, the area affected by the coseismic landslides is about 500 km^2, while some studies (e.g., Fan et al., 2018, Wu et al., 2018, and Dai et al., 2017) only mapped ~2 000 individual landslides; the actual number, very likely, has been much underestimated. Therefore, it is necessary to reexamine the relevant data and establish a more detailed inventory of the coseismic landslides related to the 2017 Jiuzhaigou Earthquake.

This study aims to build such a database by combining high-resolution remote sensing images and field investigations and to remap the spatial distribution of these landslides with respect to control factors including topography, geology, hydrology, seismology and human activities. The results of this work would help further understanding the cause of the coseismic landslides and the efforts of post-seismic hazard prevention and reduction in the affected region.

1 TECTONIC SETTING AND THE JIUZHAIGOU EARTHQUAKE

Since the Late Cenozoic era, the Indian Plate is continuing to move toward the Eurasian Plate, resulting in the present tectonic pattern of the Tibetan Plateau. From south to north, the plateau consists of four first-class active blocks: Lhasa, Qiangtang, Bayan Har and Qaidam-Qilian (Fig. 1a). Recently a series of earthquakes with magnitude larger than 6.5 occurred around the Bayan Har Block, including the 2008 Wenchuan and 2013 Lushan events on the eastern boundary, the 1997 Mani and the 2010 Yushu events on the southern boundary, the 2001 Hoh Xil Earthquake on the northern boundary and the 2008 and 2014 Yutian events on the western boundary. The 2017 M_W 6.5 Jiuzhaigou Earthquake is another one striking the northeast of the Bayan Har Block, about 250 km away from the epicenter of the 2008 Wenchuan Quake. This area hosts several active faults, such as the NS-trending reverse Minjiang, NNW-strike reverse Huya and NWW-directed strike-slip Tazang faults, all of which belong to the eastern terminal part of the East Kunlun fault zone with strong tectonic activities (Fig. 1a) (Xu et al., 2016, 2013a). It is also the transition region where the strike-slip component of the East Kunlun fault is transferred to reverse property. Historical earthquake and paleo-earthquake data indicate that few current earthquakes occurred there. Coupling with the GPS inversion results, Xu et al. (2017a, b) deduced that there is a high possibility that large-earthquakes may occur in this region.

The distribution of relocated earthquake sequence vertical to the seismogenic fault shows that the mainshock rupture was much deeper and then propagated upward; while for the distribution along the seismogenic fault, there is a seismic gap on the northwest side of the epicenter where the mainshock ruptured northwestward and southeastward respectively separating the aftershocks into two clusters. The northwestern cluster is much larger than the southeastern one. Because no obvious seismic surface rupture was found in the field and no known active faults corresponded to the earthquake sequence and seismic landslides, it is difficult to identify the seismogenic fault of the 2017 Jiuzhaigou Earthquake. Yao et al. (2017), Xu et al. (2017a) and Fang et al. (2018) suggested that it is the northern part of the Huya fault; Yi et al. (2017) named it the Shuzheng fault belonging to the East Kunlun fault zone or the Huya fault; Ren et al. (2017) considered that it is an eastern secondary fault of the Tazang fault, while Li Y S et al. (2017) insisted that the quake was generated by two NW331º faults (the seismogenic fault and its secondary fracture). Despite these disagreements including its name and affiliation, constrained by focal mechanism solutions, aftershock locations, InSAR coseismic deformation field, seismic damage distribution and the abnormal radon measurements, most researchers inferred that the seismogenic fault is an upright sinistral strike-slip fault with strike of about 330º and dip direction of SW (Fang et al., 2018; Han et al., 2018; Li Y S et al., 2017; Ren et al., 2017; Yao et al., 2017; Yi et al., 2017; Xu et al., 2017a). Therefore, this work adopts this structure (Fig. 1b, dash line), which can be used as a control factor for the landslide distribution pattern. The Carboniferous limestone distributes along the fault accounting for nearly half of the study area, followed by the Triassic sandstone and limestone mainly concentrating in the north of this region.

2 DATA AND METHOD

2.1 Remote Sensing Imagery and Landslide Identification

The high-resolution and low-cloud-coverage remote sensing images can help improve the quality of coseismic landslide inventories. We chose the images before and after the earthquake which are close to the seismic origin time and have low cloud coverage and optimal resolution, including the series of pre-seismic images on the Google Earth (GE) Platform and 0.5 m-resolution Geoeye-1 post-seismic images (shot on August 14 2017). The Google Earth Platform provides high-precision and stereoscopic images at various times and guarantees the continuity of pre-seismic images. The processed post-seismic Geoeye-1 image can overlie on the GE Platform. Thus, the image can not only provide a stereo-like perspective view, but also facilitate the comparison of the pre- and post-earthquake images. While interpreting, we followed the principles of stereo coverage images, continuous spatial distribution and polygonal individual landslides and so on (Xu, 2015; Harp et al., 2011). Based on the GE Platform, the areas with bright tones, flow-textures and no vegetable-coverage were identified as coseismic landslides and were delineated as polygons through visual interpretation and contrast of aforementioned two kinds of images (Fig. 2). Finally, combined with field surveys, repeated reviews and validations were done to reduce errors and ensure the objectivity and precision of the landslide inventory prepared.

2.2 Control Factors of the Coseismic Landslides

Five factors, i.e., topography (elevation, slope angle, slope position and slope aspect), geology (lithology), hydrology (the distance to river channels), human activity (the distance to roads) and seismology (the distance to the epicenter, the distance parallel to and vertical to the seismogenic fault) were considered when mapping the landslides triggered by the 2017 Jiuzhaigou Earthquake.

Elevation, slope angle and slope aspect were obtained based on 10 m resolution DEM which was resampled from the 30 m SRTM DEM. The elevation was divided into 12 classes with an interval of 200 m, slope angle into 7 classes with an interval of 10º. Slope aspect, which means the facing direction of a slope, was divided into 9 classes. Among them, the flat areas have no downslope direction and are horizontal with zero slope angle. To describe the relative positions and special shapes of slope surfaces, the rule suggested by Weiss (2001) was used to divide the slope position into 6 categories: ridges, upper slope, middle slope, flat slope, lower slope and valley. Here, the flat slope is an area where the elevation is close to the mean elevations of their neighborhood cells and slope angle is nearly zero (Jenness et al., 2013; Weiss, 2001).

Data of lithology were derived from digitizing a geological map on a scale of 1 : 200 000. The study area was divided into ten units of lithology as follows: (1) Pliocene (N_2): conglomerate and sandy conglomerate with little sandstone lens; (2) Upper Triassic (T_3): tuffaceous sandstone, marlite and quartz sandstone; (3) Middle Triassic (T_2): interbedded sandstone and
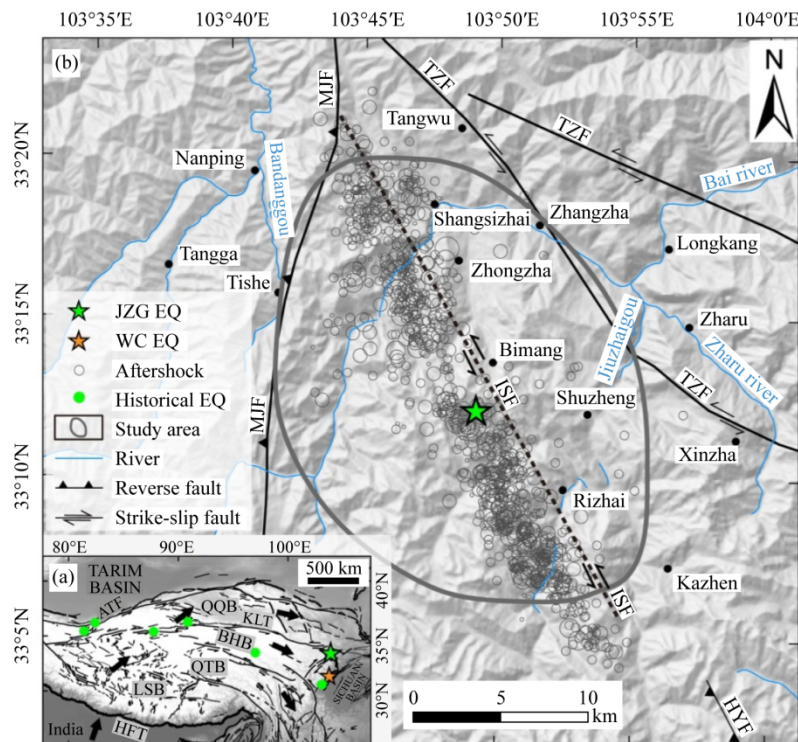

Figure 1. Tectonic setting of the 2017 Jiuzhaigou Earthquake (Xu et al., 2017a, 2013b). (a) Active blocks, major faults in the Tibetan Plateau, historical earthquakes around the Bayan Har Block (green dot) and the epicenter of the Jiuzhaigou (green star) and Wenchuan (yellow star) earthquakes. (b) Enlarged map showing regional tectonics and aftershocks (grey circle). ATF. Altyn tagh fault; HFT. Himalayan frontal thrust; KLF. Kunlun fault; QQB. Qaidam-Qilian Block; BHB. Bayan Har Block; QTB. Qiangtang Block; LSB. Lhasa Block; MJF. Minjiang fault; HYF. Huya fault; TZF. Tazang fault; ISF. inferred seismogenic fault; JZG EQ. Jiuzhaigou Earthquake; WC EQ. Wenchuan Earthquake.
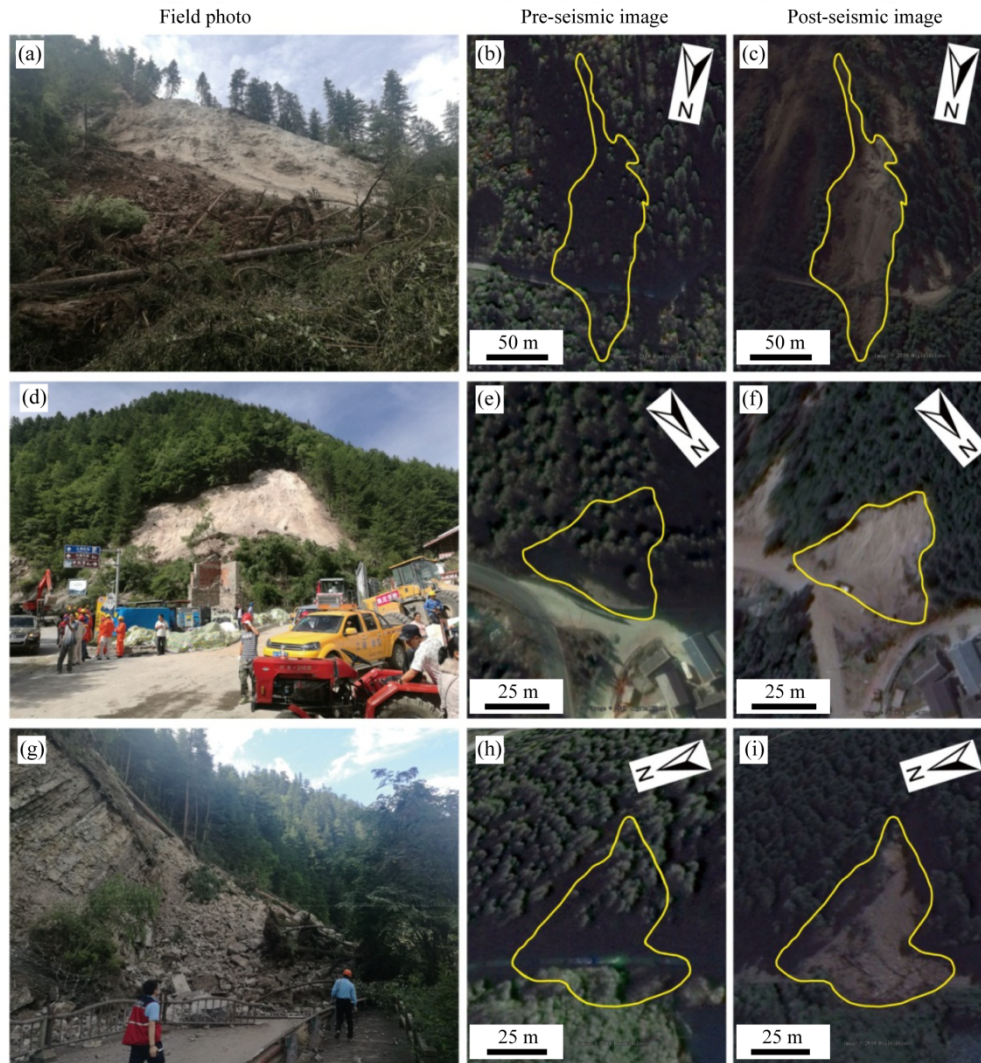
Field photo   Pre-seismic image   Post-seismic image

Figure 2. Field photos (left) and pre- (middle) and post-seismic (right) remote sensing images of three typical landslides. Yellow polygons denote boundaries of landslides. Geographical locations: (a)–(c) 103.876 6ºE, 33.156 5ºN; (d)–(f) 103.793 3ºE, 33.305 9ºN; (g)–(i) 103.885 8ºE, 33.166 7ºN.

limestone, interbedded sandstone and slate, lime dolomite; (4) Lower Triassic (T_1): argillaceous limestone, argillaceous dolomite, limestone and slate; (5) Middle Permian (P_2): limestone, shale and carbonaceous shale; (6) Lower Permian (P_1): limestone, dolomitic limestone, dolomite; (7) Upper Carboniferous (C_3): limestone intercalated dolomite and irony claystone; (8) Middle Carboniferous (C_2): limestone, oolitic limestone, crystalline limestone; (9) Lower Carboniferous (C_1): interbedded limestone and dolomite, limestone intercalated shale; and (10) Upper Devonian (D_3): organic limestone and medium layered-massive dolomite.

The roads in the study area are mostly constructed along rivers, and their excavation may reduce the slope stability. Thus the controls of the river channels and roads on the landslides were taken into account in this work. The river channels were mapped using the aforementioned 30 m resolution DEM with grid threshold of flow accumulation larger than 20 000 cells (http://resources.arcgis.com/en/help/main/10.1/index.html#/na/009z00000051000000) (O'Callaghan and Mark, 1984). The thematic maps of river channels and roads were constructed by building buffers with 1 km buffer distances.

Because of the low correlation between aftershocks and earthquake intensity and peak ground acceleration (PGA) (Xu et al., 2018b), we chose the distance to the epicenter, the distance bands parallel and vertical to the inferred seismogenic fault as seismic factors instead. They are associated with the features of earthquake rupture and energy propagation and can affect the distribution of coseismic landslides. The buffers were established around the epicenter and along the seismogenic fault with 1-km buffer interval, respectively. The bands vertical to the fault were defined in the same way along the direction normal to the fault crossing the epicenter.

3 RESULTS AND ANALYSES
3.1 Landslide Inventory

Combining visual interpretation of remote sensing images and field investigations, we finally established a more detailed landslide inventory for the 2017 Jiuzhaigou Earthquake with 4 834 coseismic landslides distributed in an area of 434 km^2 (Fig. 3). The total landslide-occupation area is 9.64 km^2, and the volume is estimated to be 80.4×10^6 m^3 according to the relation (V=1.314 7×$A^{1.208\ 5}$) (Xu et al., 2016b). The largest

landslide is 236 338.3 m^2, the smallest one is 7.8 m^2 and the average is 1 993.4 m^2. There are 189 landslides with an area larger than 10 000 m^2, 1 669 with area between 1 000–10 000 m^2; 2 469 in 100–1 000 m^2; and 507 smaller than 100 m^2. The landslide area percentage (LAP, defined as the percentage of the landslide area in each factor category) and landslide number density (LND, defined as the number in each factor category) of the study area is 2.22% and 8.83 km^{-2}, respectively. The dominant direction of landslide distribution coincides with the inferred seismogenic fault, both striking in NNW-direction.

Most of the landslides are medium- and small-scale rock falls and disrupted debris slides, few large-scale ones (Fig. 4).

Our study area is largely within the study areas of Dai et al. (2017), Fan et al. (2018) and Wu et al. (2018) (Fig. 3b). According to the comparison in Table 1, our smaller study area hosts more landslides than others, though they all have similar minimum and maximum individual landslide areas and the differences among the total areas are small as well. The inventory presented by Wu et al. (2018) consists of the landslides in the inventory of Dai et al. (2017) and Fan et al. (2018) and
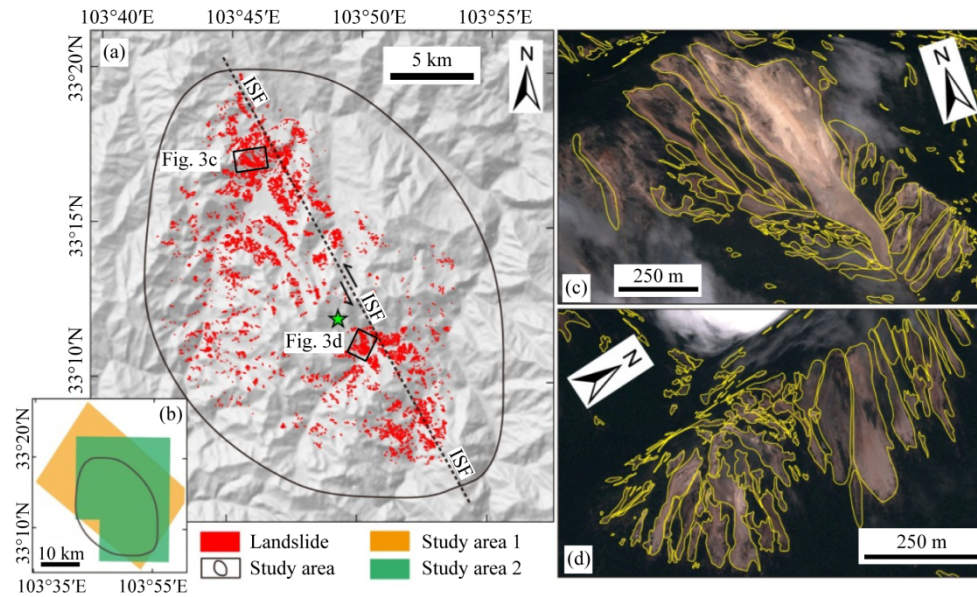

Figure 3. Study area and landslide inventory. (a) Landslide distribution related to the 2017 Jiuzhaigou Event; (b) locations of study areas of relevant studies; (c) and (d) two enlarged areas with intensely distributed landslides. The study area of this work is the ellipse in (a) and (b). Study area 1 (orange polygon in (b)) is the study area of Dai et al. (2017) and Fan et al. (2018); Study area 2 (green polygon in (b)) is the study area of Wu et al. (2018). ISF in (a) represents the inferred seismogenic fault. Red polygons in (a) are landslides mapped in this study. Yellow polygons in (c) and (d) are boundaries of individual landslides.
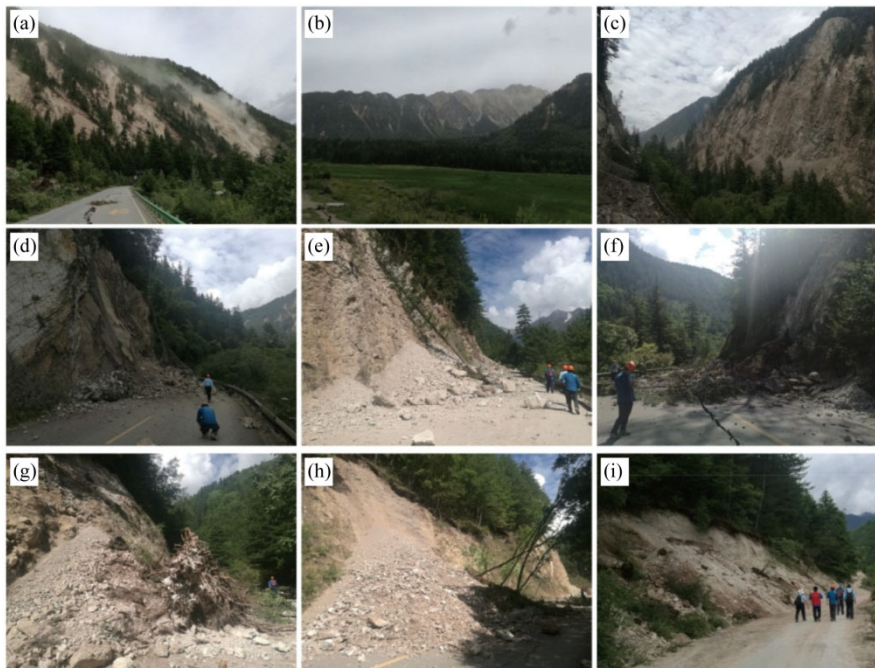

Figure 4. Field photos of typical landslides. (a)–(c) Landslide clusters in distant view; (d)–(i) individual landslides in close view.

Table 1   Comparison of relevant studies on landslides triggered by the 2017 Jiuzhaigou Earthquake

Sources	Distribution area (km²)	Landslide number	Total area (km²)	Mean area (m²)	Max. area (m²)	Min. area (m²)
Dai et al. (2017)	840	1 883	8.11	4 307	231 000	9.7
Fan et al. (2018)						
Wu et al. (2018)	1 275	2 212	11.8	5 312.9	231 297.3	9.7
This study	434	4 834	9.64	1 993.4	236 338.3	7.8

other 435 landslides in the extra area around the epicenter. The post-seismic images they used include 0.2 and 1 m aerial imageries shot on August 11, 2017, 1 and 4 m resolution Gaofen-2 images on August 9, 2017, and 1 m Gaofen-1 images on August 16, 2017 and 10 m Sentinel-2 images on September 6, 2017. Though these images together cover a large area, the scope of the high-resolution images (0.2 m aerial imageries) is small and mainly on the northeastern side of the epicenter (Fan et al., 2018; Dai et al., 2017). Nevertheless, the high-resolution Geoeye-1 image (0.5 m) nearly covering the whole meizoseismal area facilitates identification of much smaller landslides in our study. Moreover, the added landslides in our study are mainly distributed along and in the southwest part of the inferred seismogenic fault which is covered by meter-level images in other studies. On the other hand, we took much longer time to divide the complex landslides into individual ones according to principles proposed by Xu (2015). The much accurate landslide number can help obtain the approximate real landslide number density and volume and it will help better understand the seismic landslides.

3.2   Distribution Pattern of the Coseismic Landslides with Respect to Various Factors

LND is the landslide number density, which indicates the landslide concentration in each class of the control factors. LAP is short for landslide area percentage, which means the relative size of the landslides in each class of the control factors. They all reflect the spatial distribution characteristics. Using LAP and LND as indexes, we have mapped the distribution pattern of the coseismic landslides triggered by the 2017 Jiuzhaigou Earthquake with respect to various factors aforementioned.

3.2.1   Terrain

The elevation of the study area ranges from 2 072 to 4 472 m. The LAP and LND firstly increase and then decrease with the growing elevation (Figs. 5a and 5b). They peak in the range of 3 000–3 200 m with values of 4.68% and 22.50 km⁻² respectively, followed the range of 2 800–3 000 m with values of 3.64% and 19.66 km⁻². While the areas with elevations of 2 800 to 3 400 m account for 40% of the study area, 60% of the total landslides occurred there. The slope angle range of the study area is 0–79.8°, mostly in 20°–40°. The LAP and LND have positive correlations with the slope angles, especially for the slopes larger than 30°. The slopes exceeding 60° have the largest LAP and LND, 9.6% and 33.43 km⁻², respectively (Figs. 5c and 5d). As shown in Figs. 5e and 5f, most of the landslides are distributed in the upper, middle and flat slopes. The largest LAP, 2.39%, is in the class of middle slopes, which has the largest classification area. The largest LND, 12.20 km⁻², falls in the class of upper slopes, implying that this position is more prone

to slope failure. The Flat slopes tend to accumulate deposits, having a higher susceptibility to slope failure as well. The scale and number of landslides on the N, NE, E and SE-facing slopes are slightly larger than other aspects. However, except for the flat aspect, LAP and LND have a tiny fluctuation varying with the slope aspects. It means that the landsliding in the study area is not sensitive to the slope aspect, though N, NE, E and SE-facing slopes are slightly more prone to seismic failure (Figs. 5g and 5h).

3.2.2   Geology

From Figs. 6a and 6b, most of the landslides occurred in the area of Carboniferous (C) limestone and dolomite. Specifically, the largest LAP and LND are in the Middle Carboniferous (C₂) area, 4.84% and 22.39 km⁻² respectively. Accounting for 46% of the study area, the Carboniferous strata have 81% of the total landslides. Among the 189 landslides with an area larger than 10 000 m², 174 pieces occurred there. These all demonstrate that the strata of Carboniferous are most prone to landsliding.

3.2.3   River channels and roads

The correlations between river channels and LAP and LND (Figs. 7a and 7b) suggest that the landslides are most likely to generate at the places close to the river channels. LAP and LND reach their peaks (3.02% and 15.95 km⁻², respectively) in the regions within 1 km to the rivers and generally decrease with the increasing distance. The smallest classification area of regions over 4 km distant from the river channels may result in the abnormally high LAP and LND values. Figures 7c and 7d show that the closer the distance to roads is, the more the landslides are. Relatively larger values of LAP and LND appear in the regions within 2 km to the roads, implying the influence of the free surfaces resulted from road excavation on the slope's stability. The other peak values of LAP and LND are in the scope within a distance of 4–5 km away from the roads, which may indicate that other factors play more important roles in landslide distribution in the regions far away from roads.

3.2.4   Seismology

Generally, the number and scale of landslides increase with the decreasing distance to the epicenter. However, for the 2017 Jiuzhaigou Event, most of the landslides are distributed within 2–9 km to the epicenter rather than close proximity to it (Figs. 8a and 8b). Particularly, the largest values of LAP and LND are in the range of 3–4 km to the epicenter, while the lowest values are in the range within 1 km which roughly corresponds to the gap with few aftershocks. Except that the epicenter is located in the area with a post-seismic Geoeye image of more cloud coverage, this is possible because that the earth-
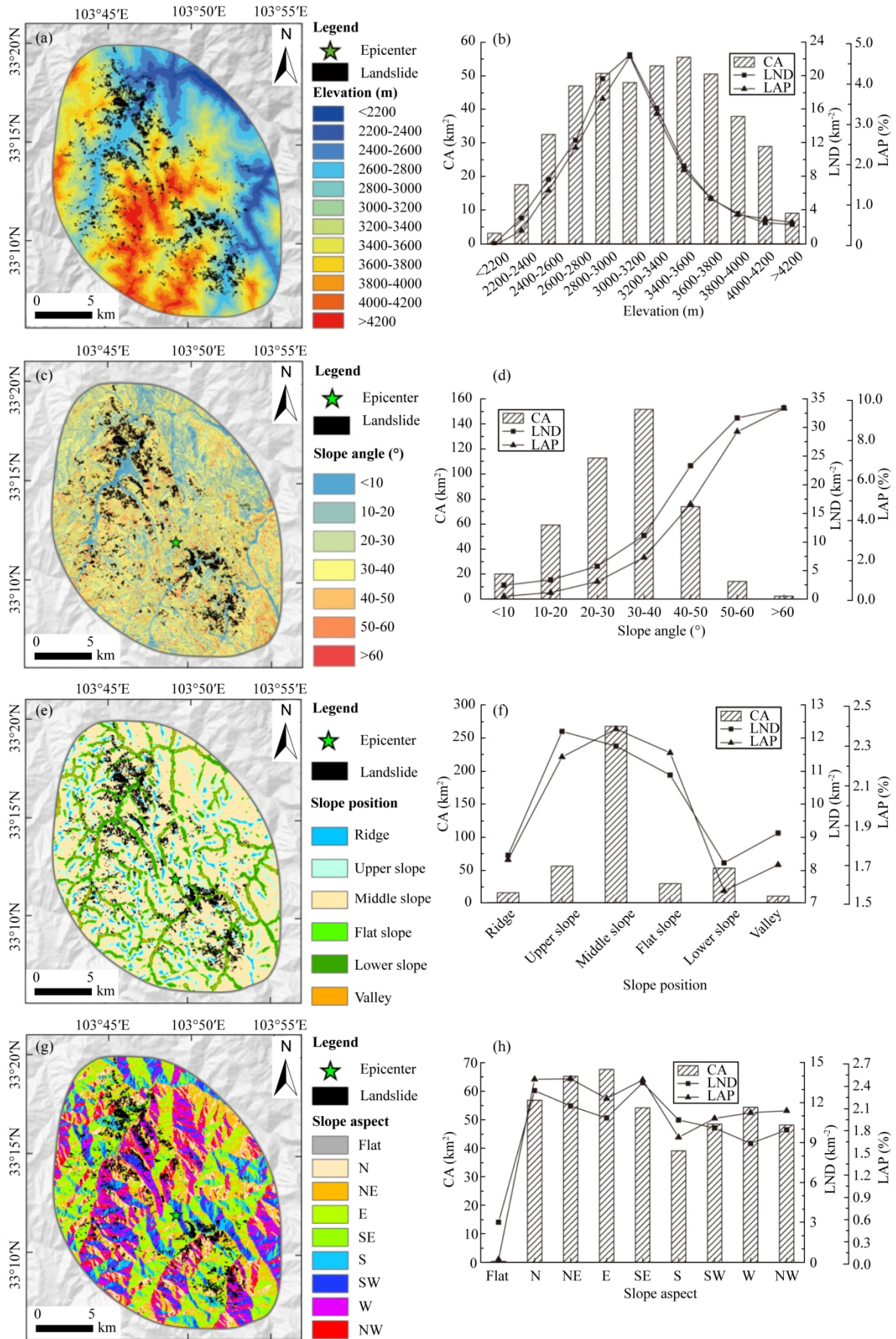
Figure 5. Classifications of terrain factors (left) and their relations with LND and LAP (right). (a) and (b) elevation; (c) and (d) slope angle; (e) and (f) slope position; (g) and (h) slope aspect. CA. Classification area; LND. landslide number density; LAP. landslide area percentage (see text for their definitions).
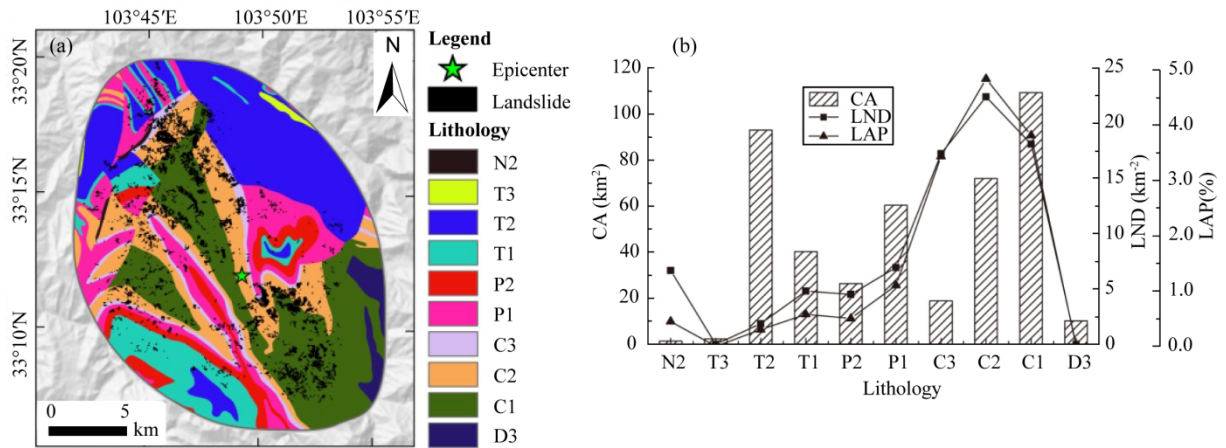
Figure 6. Classifications of lithology (a) and their relations with LND and LAP (b). CA. Classification area; LND. landslide number density; LAP. landslide area percentage (see text for their definitions).
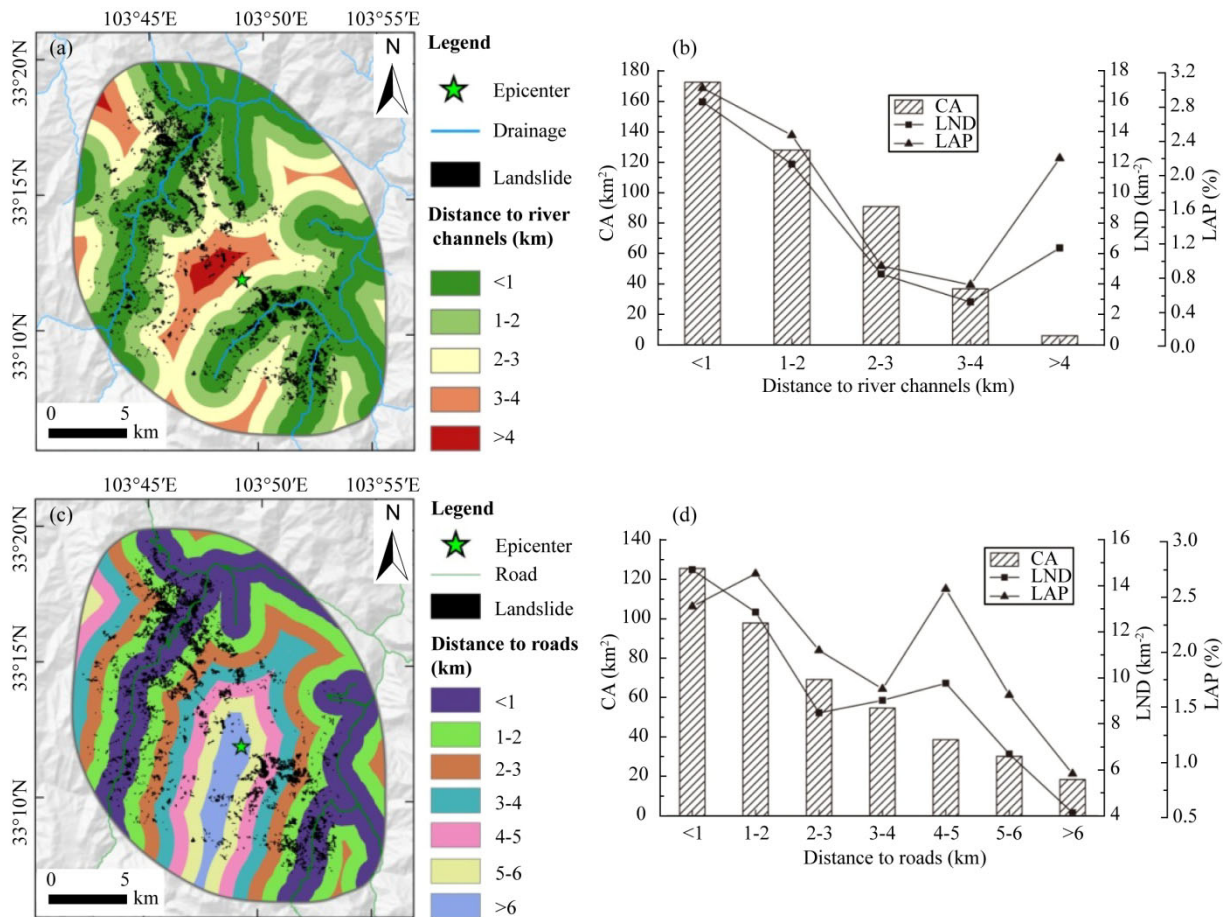

Figure 7. Classifications of river channels and roads (left) and their relations with LND and LAP (right). (a) and (b) distance to river channels; (c) and (d) distance to roads. CA. Classification area; LND. landslide number density; LAP. landslide area percentage (see text for their definitions).

quake source is relatively deep and regional elevation is high, and the epicenter is at the high slope position where the rock strength is rather large (Xu et al., 2018b). Figures 8c and 8d are the statistics of LAP and LND in the bands parallel to the inferred seismogenic fault, which reach their peaks in the bands (bands 11–13) close to the epicenter and seismogenic fault with values of 7.122% and 28.47 km^{-2}, respectively. Besides these

three bands, LAP and LND decline sharply with the increase of the distance to the epicenter and fault. The above phenomenon reveals that the landslides triggered by the Jiuzhaigou Event are concentrated along the bands in which the epicenter and fault are located, probably related to the strike-directed spreading of the source rupture (Li Y S et al., 2017). In addition, landslides induced by strike-slip earthquakes are usually symmetrically

distributed on either side of the seismogenic fault, such as the 2002 Denali Earthquake (Gorum et al., 2014) and the 2010 Yushu Earthquake (Xu and Xu, 2014a). For the Jiuzhaigou Shock, however, the landslide densities in the southwest of the fault are much larger than in the northeast (Fig. 8d). Firstly, this may result from that the remote sensing image does not cover the whole study area, especially the northeast; secondly, the asymmetric distribution of lithology along the fault may also lead to the difference of landslide density and size. Statistics of LAP and LND in the bands vertical to the inferred seismogenic

fault are shown in Figs. 8e and 8f. According to Fig. 8f, the landslide densities vary along the seismogenic fault. Instead of being concentrated around the epicenter, the majority of landslides are present in the northwestern bands 5–10 (6–10 km to the epicenter) and southeastern bands 19–20 (2–4 km to the epicenter) and 24–25 (7–9 km to the epicenter), respectively. The comparison shows that except for two band groups (bands 16 and 17, bands 9 and 24), landslide densities in the southeast are larger than those in the northwest within 4 km to the epicenter. While beyond 4 km, the pattern is opposite. Such density
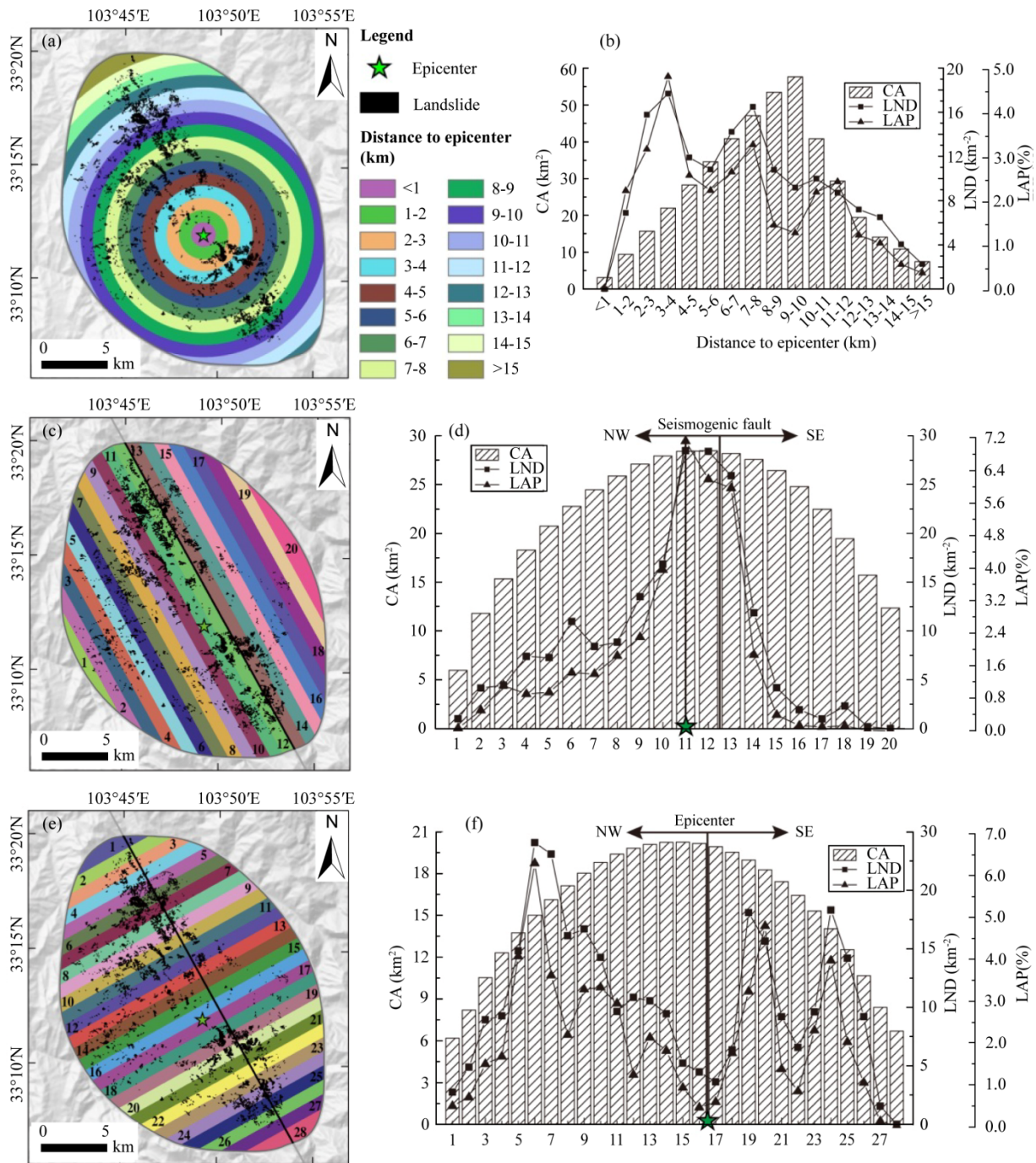

Figure 8. Classifications of seismic factors (left) and their relations with LND and LAP (right). (a) and (b) distance to the epicenter. (c) and (d) bands parallel to the fault. (e) and (f) bands vertical to the fault. Horizontal axes of (d) and (f) are the number of each band. Green stars are the epicenter of the Jiuzhaigou Event. Each band represents 1 km. CA. Classification area; LND. landslide number density; LAP. landslide area percentage (see text for their definitions).

differences in the bands vertical to the fault may indicate the varied landslide susceptibility, which can be mainly attributed to the varied rock mass strength along the fault and earthquake rupture mechanism. As mentioned before, the earthquake ruptured deeply and then simultaneously propagated to the shallow surface northwestward and southeastward. The region within 4 km to the epicenter was affected by the seismic gap between the epicenter and northwestern aftershock cluster. For the area beyond 4 km to the mainshock, the distribution of the aftershocks in the northwestern side of the epicenter is much wider and shallower than in the southeastern side (Xu et al., 2017a). Therefore, the stronger ground shaking in the northwest triggered much more landslides.

4 DISCUSSION

The incomplete landslide distribution data might mislead us in the distribution characteristics, susceptibility assessment and the further studies (Xu et al., 2014a). We compared our landslide distribution with the distribution features obtained by Fan et al. (2018) and Wu et al. (2018) which are based on different complete degrees of landslide inventories. Most of the landslide distribution patterns with the control factors are consistent, and the obvious disagreement exists in the relationship with the seismogenic fault.

The relations between lithology and LND and LAP show that the landslide-prone area is the region with strata of Carboniferous (C) limestone and dolomite which mainly distribute in the northwestern side of the fault. Besides, the northwestern wall of the fault is the hanging wall with relative thrusting component and the mass might be much weaker and easier to slide during strong shaking. The statistics in our study indicate that the seismic landslides on the northwestern wall are more than the southeastern side as well. According to the statistics of landslide area and number and the distance to fault along two profiles stated in Wu et al. (2018), the landslide area and number are much larger in the region confined by the inferred faults; moreover, the northwestern side of the fault zone has a bit more landslides than the southeastern side. However, though Fan et al. (2018) also suggested that there is an obvious difference between the distance to the fault and the landslide area percentage and number density on both sides of the inferred seismogenic fault, they thought that the northwestern wall hosted fewer landslides than southeastern one. Basically, the above disagreement is mainly due to the detail level of landslide data we used. The similar phenomenon was found by Xu et al. (2014a) that the distribution characteristics related to some factors based on incomplete landslide inventory may be not objective. Certainly, the rapid post-seismic landslide inventory is important for short-term susceptibility evaluation and disaster reduction; nevertheless, it is necessary to build a detailed landslide inventory afterward to the long-term post-disaster reconstruction and further study of understanding the general mechanism.

5 CONCLUSIONS

This work attempted to prepare a more detailed inventory of the coseismic landslides triggered by the 2017 M_W 6.5 Jiuzhaigou Earthquake, China to provide objective supporting data for subsequence research. It was based on high-resolution remote sensing imageries before and after this quake, coupled with field investigations. The resultant database permits mapping the landslides in an elliptical region surrounding the epicenter covering an area of 434 km². Totally, 4 834 landslides were counted by visual interpretation and field investigations. They occupy an area of 9.64 km², mostly medium- and small-sized rock falls and debris slides. This corroborate that the existing studies have really underestimated the landslide number and the sub-meter high-resolution images (0.5 m Geoeye-1 image) help to identify more landslides.

Using this inventory, statistics were made to characterize their distributions with respect to five primary control factors, including factors of terrain, geology, seismology, hydrology and human activity. The results show that the landsliding was insensitive to slope aspect. The majority of the coseismic landslides are in scopes of the elevation 2 800–3 400m, slope angle larger than 30º, upper, middle and flat slopes as relative slope positions, and strata of Carboniferous limestone and dolomite. Along the river channels and roads in the study area, there exist many coseismic landslides. Relatively large landslide densities along the inferred seismogenic fault suggest that it exerted a much more impressive influence on the pattern of the coseismic landslides than the location of the epicenter. Moreover, the differences in landslide densities along the inferred seismogenic fault indicate the varied landslide susceptibility. Thus, the distribution pattern of the landslides triggered by the 2017 Jiuzhaigou Earthquake was primarily controlled by the seismogenic structure, terrain, lithology, hydrology and human activity. Although this study presents an inventory covering the meizoseismal area and delineates the overall distribution pattern of the coseismic landslides and some landslides are probably omitted because of limited quality and coverage of post-seismic satellite images, the landslide data could help us further understand the landslide distribution pattern and mechanism and provide data support for the subsequence research.

REFERENCES CITED

Chigira, M., Yagi, H., 2006. Geological and Geomorphological Characteristics of Landslides Triggered by the 2004 Mid Niigta Prefecture Earthquake in Japan. *Engineering Geology*, 82(4): 202–221. https://doi.org/10.1016/j.enggeo.2005.10.006

Dai, L. X., Xu, Q., Fan, X. M., et al., 2017. A Preliminary Study on Remote Sensing Interpretation of Landslides Triggered by Jiuzhaigou Earthquake in Sichuan on August 8th, 2017 and Their Spatial Distribution Patterns. *Journal of Engineering Geology*, 25(4): 1151–1164 (in Chinese with English Abstract)

Fan, X. M., Scaringi, G., Xu, Q., et al., 2018. Coseismic Landslides Triggered by the 8th August 2017 M_S 7.0 Jiuzhaigou Earthquake (Sichuan, China): Factors Controlling Their Spatial Distribution and Implications for the Seismogenic Blind Fault Identification. *Landslides*, 15(5): 967–983. https://doi.org/10.1007/s10346-018-0960-x

Fang, L. H., Wu, J. P., Su, J. R., et al., 2018. Relocation of Mainshock and Aftershock Sequence of the M_S 7.0 Sichuan Jiuzhaigou Earthquake. *Chinese Science Bulletin*, 63(7): 649–662. https://doi.org/10.1360/n972017-01184

Feng, H. J., Zhou, A. G., Tang, X. M., et al., 2016. Development and Distribution Characteristics of Debris Flow in Zhejiang Province and Its Regional Forecast. *Earth Science—Journal of China University of Geosciences*, 42(9): 1637–1646 (in Chinese with English Abstract)

Gorum, T., Korup, O., van Westen, C. J., et al., 2014. Why so Few? Landslides Triggered by the 2002 Denali Earthquake, Alaska. *Quaternary Science Reviews*, 95: 80–94. https://doi.org/10.1016/j.quascirev.2014.04.032

Han, L. B., Cheng, J., An, Y. R., et al., 2018. Preliminary Report on the 8 August 2017 M_S 7.0 Jiuzhaigou, Sichuan, China, Earthquake. *Seismological Research Letters*, 89(2A): 557–569. https://doi.org/10.1785/0220170158

Harp, E. L., Jibson, R. W., 1996. Landslides Triggered by the 1994 Northridge, California, Earthquake. *Bulletin of the Seismological Society of America*, 86: S319–S332

Harp, E. L., Keefer, D. K., Sato, H. P., et al., 2011. Landslide Inventories: The Essential Part of Seismic Landslide Hazard Analyses. *Engineering Geology*, 122(1/2): 9–21. https://doi.org/10.1016/j.enggeo.2010.06.013

Jenness, J., Brost, B., Beier, P., 2013. Land Facet Corridor Designer: Extension for ArcGIS. Jenness Enterprises. [2018-11-10]. http://www.jennessent.com/arcgis/land_facets.htm

Kamp, U., Growley, B. J., Khattak, G. A., et al., 2008. GIS-Based Landslide Susceptibility Mapping for the 2005 Kashmir Earthquake Region. *Geomorphology*, 101(4): 631–642. https://doi.org/10.1016/j.geomorph.2008.03.003

Kargel, J. S., Leonard, G. J., Shugar, D. H., et al., 2016. Geomorphic and Geologic Controls of Geohazards Induced by Nepals 2015 Gorkha Earthquake. *Science*, 351(6269): aac8353. https://doi.org/10.1126/science.aac8353

Keefer, D. K., 1984. Landslides Caused by Earthquakes. *Geological Society of America Bulletin*, 95: 406–421

Keefer, D. K., Wartman, J., Navarro Ochoa, C., et al., 2006. Landslides Caused by the *M* 7.6 Tecomán, Mexico Earthquake of January 21, 2003. *Engineering Geology*, 86(2/3): 183–197. https://doi.org/10.1016/j.enggeo.2006.02.017

Lee, C. T., 2013. Re-Evaluation of Factors Controlling Landslides Triggered by the 1999 Chi-Chi Earthquake. In: Ugai, K., Yagi, H., Wakai, A., eds., Earthquake-Induced Landslides. Springer, Berlin Heidelberg. 213–224

Li, F., Mei, H. B., Wang, W. S., et al., 2017. Rainfall-Induced Meteorological Early Warning of Geo-Hazards Model: Application to the Monitoring Demonstration Area in Honghe Prefecture, Yunnan Province. *Earth Science—Journal of China University of Geosciences*, 42(9): 1637–1646 (in Chinese with English Abstract)

Li, Y. S., Huang, C., Yi, S. J., et al., 2017. Study on Seismic Fault and Source Rupture Tectonic Dynamic Mechanism of Jiuzhaigou M_S 7.0 Earthquake. *Journal of Engineering Geology*, 25(4): 1141–1150 (in Chinese with English Abstract)

Liao, H. W., Lee, C. T., 2000. Landslides Triggered by the Chi-Chi Earthquake. In: Proceedings of the 21st Asian Conference on Remote Sensing, Taipei. 1/2: 383–388

Liu, J. M., Wang, T., Shi, J. S., et al., 2017. Emergency Rapid Assessment of Landslides Induced by the Jiuzhaigou M_S 7.0 Earthquake, Sichuan, China. *Journal of Geomechanics*, 23(5): 639–645 (in Chinese with English Abstract)

O'Callaghan, J. F., Mark, D. M., 1984. The Extraction of Drainage Networks from Digital Elevation Data. *Computer Vision, Graphics, and Image Processing*, 28(3): 323–344. https://doi.org/10.1016/s0734-189x(84)80011-0

Owen, L. A., Kamp, U., Khattak, G. A., et al., 2008. Landslides Triggered by the 8 October 2005 Kashmir Earthquake. *Geomorphology*, 94(1/2): 1–9. https://doi.org/10.1016/j.geomorph.2007.04.007

Rao, G., Cheng, Y. L., Lin, A. M., et al., 2017. Relationship between Landslides and Active Normal Faulting in the Epicentral Area of the AD 1556 *M*~8.5 Huaxian Earthquake, SE Weihe Graben (Central China). *Journal of Earth Science*, 28(3): 545–554. https://doi.org/10.1007/s12583-017-0900-z

Ren, J. J., Xu, X. W., Zhang, S. M., et al., 2017. Tectonic Transformation at the Eastern Termination of the Eastern Kunlun Fault Zone and Seismogenic Mechanism of the 8 August 2017 Jiuzhaigou M_S 7.0 Earthquake. *Chinese Journal of Geophysics*, 60: 4027–4045 (in Chinese with English Abstract)

Tian, Y. Y., Xu, C., Chen, J., et al., 2017a. Spatial Distribution and Susceptibility Analyses of Pre-Earthquake and Coseismic Landslides Related to the M_S 6.5 Earthquake of 2014 in Ludian, Yunan, China. *Geocarto International*, 32(9): 978–989. https://doi.org/10.1080/10106049.2016.1232316

Tian, Y. Y., Xu, C., Chen, J., et al., 2017b. Geometrical Characteristics of Earthquake-Induced Landslides and Correlations with Control Factors: A Case Study of the 2013 Minxian, Gansu, China, M_W 5.9 Event. *Landslides*, 14(6): 1915–1927. https://doi.org/10.1007/s10346-017-0835-6

Tian, Y. Y., Xu, C., Xu, X. W., et al., 2016. Detailed Inventory Mapping and Spatial Analyses to Landslides Induced by the 2013 M_S 6.6 Minxian Earthquake of China. *Journal of Earth Science*, 27(6): 1016–1026. https://doi.org/10.1007/s12583-016-0905-z

Wang, H. B., Sassa, K., Xu, W. Y., 2007. Analysis of a Spatial Distribution of Landslides Triggered by the 2004 Chuetsu Earthquakes of Niigata Prefecture, Japan. *Natural Hazards*, 41(1): 43–60. https://doi.org/10.1007/s11069-006-9009-x

Weiss, A., 2001. Topographic Position and Landforms Analysis. Poster Presentation, ESRI User Conference, San Diego, CA

Wu, C. H., Cui, P., Li, Y. S., et al., 2018. Seismogenic Fault and Topography Control on the Spatial Patterns of Landslides Triggered by the 2017 Jiuzhaigou Earthquake. *Journal of Mountain Science*, 15(4): 793–807. https://doi.org/10.1007/s11629-017-4761-9

Xu, C., 2015. Preparation of Earthquake-Triggered Landslide Inventory Maps Using Remote Sensing and GIS Technologies: Principles and Case Studies. *Geoscience Frontiers*, 6(6): 825–836. https://doi.org/10.1016/j.gsf.2014.03.004

Xu, C., 2018. Landslide Seismology Geology: A Sub-Discipline of Environmental Earth Sciences. *Journal of Engineering Geology*, 26(1): 207–222 (in Chinese with English Abstract)

Xu, C., Ma, S. Y., Tan, Z. B., et al., 2018a. Landslides Triggered by the 2016 *M*j 7.3 Kumamoto, Japan, Earthquake. *Landslides*, 15(3): 551–564. https://doi.org/10.1007/s10346-017-0929-1

Xu, C., Wang, S. Y., Xu, X. W., et al., 2018b. A Panorama of Landslides Triggered by the August 8, 2017 Jiuzhaigou, Sichuan M_S 7.0 Earthquake. *Seismology and Geology*, 40(1): 232–260 (in Chinese with English Abstract)

Xu, C., Xu, X. W., 2014a. Statistical Analysis of Landslides Caused by the M_W 6.9 Yushu, China, Earthquake of April 14, 2010. *Natural Hazards*, 72(2): 871–893. https://doi.org/10.1007/s11069-014-1038-2

Xu, C., Xu, X. W., 2014b. The Spatial Distribution Pattern of Landslides Triggered by the 20 April 2013 Lushan Earthquake of China and Its Implication to Identification of the Seismogenic Fault. *Chinese Science Bulletin*, 59(13): 1416–1424. https://doi.org/10.1007/s11434-014-0202-0

Xu, C., Xu, X. W., Tian, Y. Y., et al., 2016a. Two Comparable Earthquakes Produced Greatly Different Coseismic Landslides: The 2015 Gorkha, Nepal and 2008 Wenchuan, China Events. *Journal of Earth Science*, 27(6): 1008–1015. https://doi.org/10.1007/s12583-016-0684-6

Xu, C., Xu, X. W., Shen, L. L., et al., 2016b. Optimized Volume Models of Earthquake-Triggered Landslides. *Scientific Reports*, 6(1): 29797. https://doi.org/10.1038/srep29797

Xu, C., Xu, X. W., Shyu, J. B. H., 2015. Database and Spatial Distribution of Landslides Triggered by the Lushan, China M_W 6.6 Earthquake of 20 April 2013. *Geomorphology*, 248: 77–92. https://doi.org/10.1016/j.geomorph.2015.07.002

Xu, C., Xu, X. W., Yao, X., et al., 2014a. Three (Nearly) Complete Inventories of Landslides Triggered by the May 12, 2008 Wenchuan M_W 7.9 Earthquake of China and Their Spatial Distribution Statistical Analysis. *Landslides*, 11(3): 441–461. https://doi.org/10.1007/s10346-013-0404-6

Xu, C., Xu, X. W., Shyu, J. B. H., et al., 2014b. Landslides Triggered by the 22 July 2013 Minxian-Zhangxian, China, M_W 5.9 Earthquake: Inventory Compiling and Spatial Distribution Analysis. *Journal of Asian Earth Sciences*, 92: 125–142. https://doi.org/10.1016/j.jseaes.2014.06.014

Xu, X. W., Chen, G. H., Wang, Q. X., et al., 2017a. Discussion on Seismogenic Structure of Jiuzhaigou Earthquake and Its Implication for Current Strain State in the Southeastern Qinghai-Tibet Plateau. Chinese. *Journal of Geophysics*, 60(10): 4018–4026 (in Chinese with English Abstract)

Xu, X. W., Wu, X. Y., Yu, G. H., et al., 2017b. Seismo-Geological Signatures for Indentifying $M \geq 7.0$ Earthquake Risk Areas and Their Premilimary Application in Mainland China. *Seismology and Geology*, 39(2): 219–275 (in Chinese with English Abstract)

Xu, X. W., Chen, G. H., Yu, G. H., et al., 2013a. Seismogenic Structure of Lushan Earthquake and Its Relationship with Wenchuan Earthquake. *Earth Science Frontiers*, 20(3): 11–20 (in Chinese with English Abstract)

Xu, X. W., Tan, X. B., Yu, G. H., et al., 2013b. Normal- and Oblique-Slip of the 2008 Yutian Earthquake: Evidence for Eastward Block Motion, Northern Tibetan Plateau. *Tectonophysics*, 584: 152–165. https://doi.org/10.1016/j.tecto.2012.08.007

Xu, X. W., Han, Z. J., Yang, X. P., et al., 2016. Seismotectonic Map in China and Its Adjacent Regions. Seismological Press, Beijing (in Chinese)

Yang, W. T., Qi, W. W., Wang, M., et al., 2017. Spatial and Temporal Analyses of Post-Seismic Landslide Changes near the Epicentre of the Wenchuan Earthquake. *Geomorphology*, 276: 8–15. https://doi.org/10.1016/j.geomorph.2016.10.010

Yao, X., Zhang, Z. K., Li, L. J., et al., 2017. InSAR Co-Seismic Deformation of 2017 Jiuzhaigou Earthquake and Discussions on Seismogenic Tectonics. *Journal of Geomechanics*, 23: 507–514 (in Chinese with English Abstract)

Yi, G. X., Long, F., Liang, M. J., et al., 2017. Focal Mechanism Solutions and Seismogenic Structure of the 8 August 2017 M 7.0 Jiuzhaigou Earthquake and Its Aftershocks, Northern Sichuan. *Chinese Journal of Geophysics*, 60(10): 4083–4097 (in Chinese with English Abstract)

Zhou, J. W., Lu, P. Y., Hao, M. H., 2016. Landslides Triggered by the 3 August 2014 Ludian Earthquake in China: Geological Properties, Geomorphologic Characteristics and Spatial Distribution Analysis. *Geomatics, Natural Hazards and Risk*, 7(4): 1219–1241. https://doi.org/10.1080/19475705.2015.1075162

Zuo, R. G., Carranza, E. J. M., 2017. A Fractal Measure of Spatial Association between Landslides and Conditioning Factors. *Journal of Earth Science*, 28(4): 588–594. https://doi.org/10.1007/s12583-017-0772-2